Research Article | Vol. 27, No. 12 | 10 Jun 2019 | OPTICS EXPRESS 17122
Optics EXPRESS

Tuning behaviour of slotted vernier widely tunable lasers

M. J. WALLACE,[1,2,*] GAURAV JAIN,[1] ROBERT MCKENNA,[1] FRANK BELLO,[1,3,4] AND J. F. DONEGAN[1,2,3,4]

[1]School of Physics, Trinity College Dublin, Ireland
[2]Future Networks and Communications (CONNECT), Trinity College Dublin, Ireland
[3]Centre for Research on Adaptive Nanostructures and Nanodevices (CRANN), Trinity College Dublin, Ireland
[4]Advanced Materials and BioEngineering Centre (AMBER), Trinity College Dublin, Ireland
[*]wallacmj@tcd.ie

Abstract: A detailed thermo-optic model combining the 1D transfer matrix method and a 3D finite element method is developed and used to simulate a widely tunable vernier laser based on surface etched slots. The model is used to investigate the experimentally observed tuning patterns. At low injection currents, carrier tuning dominates, while at high currents, thermal tuning is the dominant mechanism. These lasers are very simple to fabricate and have a wide tuning over 50 nm, but SMSR and linewidth performance is not yet optimised. Simulations give an insight into the observed tuning efficiency and linewidth performance of the lasers, with high carrier densities in the grating regions being identified as a key area, which is presently limiting these parameters.

1. Introduction

Widely wavelength tunable lasers are key light sources used in various technologies such as wavelength-division multiplexing (WDM) systems and gas sensing. One such tunable laser, sampled grating distributed Bragg reflector (SG-DBR) lasers demonstrate wide tunability covering the C-band with high SMSR $\geq$ 30 dB [1]. Digital supermode (DS)-DBR lasers have also achieved wide tunability with similarly high SMSR [2]. Although such lasers have achieved wide use in optical communications they generally involve complex fabrication. Much research has gone into optimizing the performance of these devices and for areas outside WDM, new device concepts must be devised which will deliver a higher yield and simpler fabrication.

In order to reduce complexity of the device fabrication, a key area of interest which has emerged is replacing embedded gratings with surface etched gratings. This removes the need for re-growth, reducing mask layer numbers and in turn simplifying the process flow. Such surface etched gratings have been successfully used to fabricated numerous lasers such as single mode DFBs [3]. More recently, a monolithic PIC comprised of tunable single mode lasers, semiconductor optical amplifiers (SOAs) and multi-mode interference (MMI) couplers, using a simple slotted grating design was demonstrated [4]. Widely tunable lasers have also been demonstrated using a monolithic slotted grating design, demonstrating linewidth $\leq$ 800 kHz and fast wavelength switching between channels.

Research into monolithic laser designs with simple fabrication has been previously undertaken within our group. From this research a platform for simply fabricated laser diodes based on surface etched gratings has been developed. The gratings are high order and are formed through etching slots in the ridge of the laser waveguide. We have developed single mode lasers integrated with SOAs and electro absorption modulators (EAM) [5, 6], as well as laser arrays covering the C-band [7]. Using this slotted grating structure a vernier laser based on slots, analogous to the SG-DBR laser, has also been demonstrated achieving > 50 nm tuning range with SMSR > 30 dB

#359909 https://doi.org/10.1364/OE.27.017122
Journal © 2019 Received 12 Feb 2019; revised 4 Apr 2019; accepted 29 Apr 2019; published 4 Jun 2019

Optics EXPRESS

for the majority of this range [8].

Previous work examined the tuning behaviour of single mode slotted laser, predicting thermal tuning using experimentally fitted trends or analytic models [9, 10]. In this paper, a numerical thermo-optic model capable of simulating the tuning behaviour is developed and compared with experimentally observed tuning. Such a model is essential in understanding the tuning and looking towards a way to improve the performance.

2. Laser design and operation

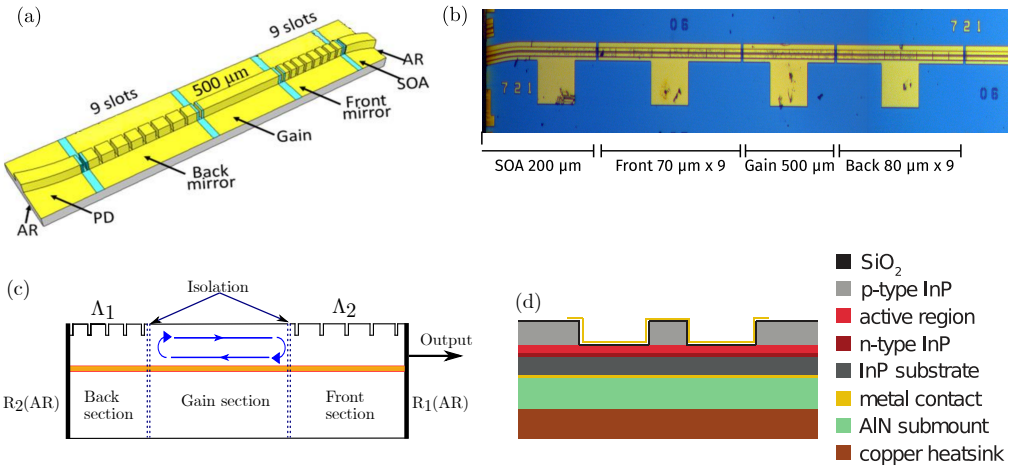

Fig. 1. Slotted vernier laser. (a) Schematic, (b) optical image with different sections indicated underneath, 2D schematic detailing cavity structure and (d) epitaxy of the three section laser, showing the ridge waveguide in the centre.

Figure 1 shows a schematic of the slotted laser structure featuring the high order surface etched grating, which has been described in [8] and [11]. The orders of the front and back gratings are 278 and 328 respectively. The schematic of the laser can be seen in Fig. 1(a), with an optical image provided in Fig. 1(b). The 2 µm wide ridge waveguide is split into five sections: a back and front grating which surround a gain section, forming the laser cavity, an SOA at the output facet and a photo detector (PD) section. The 200 µm SOA is curved at 7° to reduce the reflection from the front facet. An anti-reflection (AR) coating is applied to the back and front facet to avoid feedback. The cavity schematic can be seen in Fig. 1(c). The slots used to form the grating are 1.0 µm wide and 1.85 µm deep, the same as the ridge height. Gratings in the slotted vernier laser are active, as opposed to conventional SG-DBR laser in which the gratings are passive.

The period of the front and back grating are chosen such that each grating has a different FSR which allows one to tune between supermodes. The FSR is given as,

$$\Delta\lambda = \frac{\lambda^2}{2n_g\Lambda}, \tag{1}$$

where n_g is the group refractive index, Λ is the grating period and λ is the laser wavelength. Figure 2 shows the resulting reflection peaks for the front and back gratings simulated using the 2D-scattering matrix method (SMM) [12]. By tuning one grating relative to the other the vernier effect can be exploited.

The epitaxial structure, shown inset in Fig. 1(d), contains an active region consisting of five AlGaInAs quantum wells with an emission peak at ~ 1545 *nm*. Above this are a 1.6 *µm* thick

Optics EXPRESS

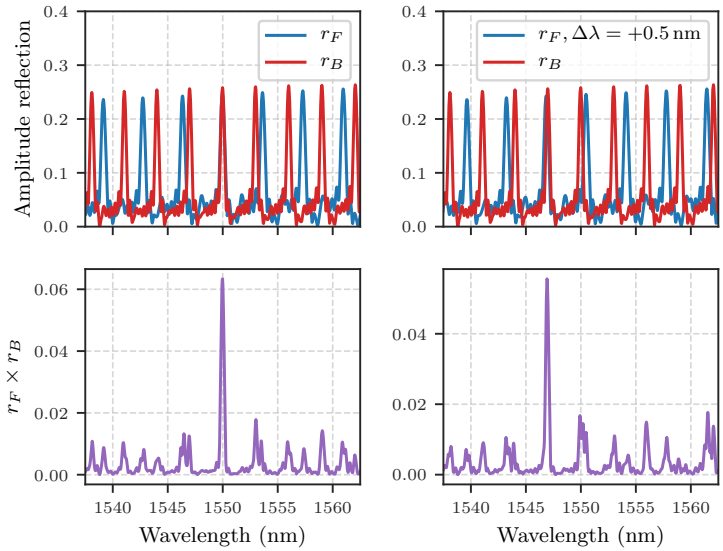

Fig. 2. Illustration of the Vernier effect: Top: reflection spectra produced by gratings with different periods at front and back. Bottom: the spectra of the combined front and back spectra from the top showing the large change in lasing wavelength.

p-doped InP layer, 50 *nm*-thick, p-doped InGaAsP layer, and a 200 nm InGaAs contact layer. The laser samples were fabricated by CST Global Ltd. The laser fabrication process involves forming the ridge and slots via an inductively coupled plasma (ICP) etch using Cl_2 and N_2 gas, after which the laser ridge is passivated and metal contacted. The laser is subsequently coated with anti-reflection (AR) films on both facets, before being eutectic bonded onto an AlN carrier. It should be noted that the lasers in the current study do in fact use e-beam lithography to form the grating patterns due to the lack of an i-line stepper in the foundry, but this is not a technical requirement of the device fabrication.

3. Modelling and simulation theory

The dominant tuning mechanisms in such laser diodes are free carrier plasma tuning and thermal tuning. In order to accurately model the tuning of slotted vernier lasers a model which accounts for both effects is necessary. Free carrier plasma tuning can be calculated by solving for the carrier density profile within the cavity. This is achieved via the time-domain transfer matrix method (TDTMM) from which lasing wavelength and SMSR are also extracted.

In order to accurately model the thermal tuning, including thermal transfer between sections of the laser, it is necessary to solve the heat equation in 3D. This is achieved using open source 3D finite element method (FEM) solver FEniCS to solve for the heat equations [13, 14].

The model first solves for the photon and carrier density profiles within the laser cavity. These profiles feed into the heat equations which are solved using the FEM. The temperature profiles as solved via the FEM can then be used in the TDTMM to fully account for thermal effects.

Optics EXPRESS

3.1. Time-domain transfer matrix method

The static transfer matrix relates the backward and forward travelling fields at one port to that of another, given by

$$\begin{bmatrix} E_F(k+1) \\ E_B(k+1) \end{bmatrix} = \begin{bmatrix} A_k \end{bmatrix} \begin{bmatrix} E_F(k) \\ E_B(k) \end{bmatrix}, \tag{2}$$

where E_F and E_B are the forward and backwards travelling fields respectively, and A_k is the 2x2 transfer matrix [15].

Equation (2) describes the static case where we are simply relating the field at one side of the cavity to the other. The TD-TMM requires the transfer matrix to relate the forward and backward travelling fields both spatially and temporally [16]. This is achieved by writing the transfer matrix in a time dependent form,

$$\begin{bmatrix} E_F(t+\Delta t, k+1) \\ E_B(t, k+1) \end{bmatrix} = \begin{bmatrix} A_k \end{bmatrix} \begin{bmatrix} E_F(t, k) \\ E_B(t+\Delta t, k) \end{bmatrix}. \tag{3}$$

Multiplying the right-hand side out gives

$$\begin{aligned} E_F(t+\Delta t, k+1) &= a_{11}(t,k)E_F(t,k) + a_{12}(t,k)E_B(t+\Delta t, k) \\ E_B(t, k+1) &= a_{21}(t,k)E_F(t,k) + a_{22}(t,k)E_B(t+\Delta t, k), \end{aligned} \tag{4}$$

where $a_{i,j}$ are the elements of the transfer matrix A_k. In order to formulate the left hand side of the equation in terms of $(t+\Delta t)$ the equation is re-arranged as follows:

$$\begin{aligned} E_F(t+\Delta t, k+1) &= a_{11}(t,k)E_F(t,k) + a_{12}(t,k)E_B(t+\Delta t, k) \\ E_B(t+\Delta t, k) &= (E_B(t, k+1) - a_{21}(t,k)E_F(t,k))/a_{22}(t,k). \end{aligned} \tag{5}$$

The transfer matrix for homogeneous subsections is given by

$$A_{gain} = \begin{bmatrix} \exp(i\beta z) & 0 \\ 0 & \exp(-i\beta z) \end{bmatrix}, \tag{6}$$

in which the propagation constant is

$$\beta = n_{eff}k_0 + i(\Gamma g - \alpha_i)/2, \tag{7}$$

where n_{eff} is the effective index, k_0 is the wave vector, Γ is the confinement factor, g is the gain and α_i is the intrinsic loss. The transfer matrix for a reflective interface produced by a slot is constructed as the transfer matrix for the slot multiplied by the adjacent homogeneous subsection as follows:

$$A_{slot} = \frac{1}{t}\begin{bmatrix} 1 & -r \\ r & t^2 - r^2 \end{bmatrix} \begin{bmatrix} \exp[iz(\beta - i\alpha_s/2)] & 0 \\ 0 & \exp[-iz(\beta - i\alpha_s/2)] \end{bmatrix}, \tag{8}$$

where r and t represent the reflection and transmission of the interface respectively and are related as

$$t = \sqrt{1 - r^2}. \tag{9}$$

The term α_s then accounts for the loss of the slot. The reflectivity and transmission of the grating structure is first simulated using the 2D scattering matrix method (2D-SMM) as discussed in [12].

Optics EXPRESS

The individual slot values for r and α_s are subsequently fitted such that the 1D-TMM reflection and transmission spectra matches the 2D-SMM spectra. In this way loss from the grating is accurately reproduced in the model. The amplitude reflection and transmission of the front and back gratings are simulated to be ~ 0.23 and 0.5 respectively.

The rate of spontaneous emission per unit time is formulated as random Gaussian noise satisfying the correlation

$$\begin{aligned}\langle s_{F,B}(t,k)s^{*}_{F,B}(k^{'},t^{'})\rangle &= \frac{\beta_g(BN^2)v_g}{\nu_{sp}}\delta(k-k^{'})\delta(t-t^{'}),\\ \langle s_{F,B}(t,k)s_{F,B}(k^{'},t^{'})\rangle &= 0,\end{aligned} \tag{10}$$

where β_g the geometric spontaneous coupling factor which determines the fraction of spontaneous emission coupled from the quantum wells into the waveguide, B is the bimolecular recombination coefficient, N is the carrier density, and ν_{sp} is the bandwidth of the spontaneous emission, taken as 12.49 THz (100 nm), typical for such devices [15]. The $\langle\rangle$ operator is the time averaged mean.

In conjunction with solving for the propagating waves, we also need to solve for the photon and carrier densities, gain and spontaneous emission within each discrete subsection in the simulation. The photon density is given by the solution of the optical field in each subsection

$$S_k = (|E_{F,k}|^2 + |E_{B,k}|^2)/v_g. \tag{11}$$

The carrier density in each subsection is then updated as

$$N(t+\Delta t,k) = N(t,k) + \Delta t[\eta\frac{I(t,k)}{qV} - R(N(t,k)) - v_g g(t,k)S_k], \tag{12}$$

where η_i is the injection efficiency, I is the injection current, q is electron charge, V is the active region volume, g is the gain per unit length, R is the rate of spontaneous recombination given by

$$R(N) = AN + BN^2 + CN^3, \tag{13}$$

where A is the non-radiative linear recombination, B is the bimolecular recombination and C is Auger recombination coefficient. In order to include thermal effects we take the same approach as [17] by adjusting Eq. (13) with a characteristic temperature T_0 which takes into account changes in $R(N)$ with temperature as follows:

$$R(N) = \exp[\gamma(\frac{1}{T_0} - \frac{1}{T})] \cdot (AN + BN^2 + CN^3), \tag{14}$$

$$\gamma = \frac{E_A}{k_B}, \tag{15}$$

where $E_A = 0.06$ eV is the activation energy taken from [18] and k_B is Boltzmann's constant.

The gain is approximated as a linear function of carrier density set relative to the carrier density at transparency N_o, given by

$$g(N_k,S_k) = \frac{T_0}{T}\frac{dg}{dN}\frac{(N_k - \frac{T}{T_0}N_o)}{1+\epsilon S_k}, \tag{16}$$

where $\epsilon = \epsilon_0\Gamma$ and ϵ_0 is the fundamental saturation coefficient. dg/dN is the differential gain and gives the rate of change of gain with carrier density. We have again adopted the approach from [17] to account for changes in dg/dN and N_0 with temperature.

As we are modelling laser tuning over the C-band, it is necessary take gain dispersion across this wavelength range into account. As this model is working in the time domain, we make use

Optics EXPRESS

of an infinite impulse response digital filter (IIR) to model gain dispersion. In this model we use the same Lorentzian filter used by [19], which has a frequency response of the form

$$|\mathcal{H}(\omega)|^2 = \frac{(1-\eta)^2}{1+\eta^2-2\eta\cos[(\omega+\delta_g dt)]}, \tag{17}$$

where $0 \leq \eta \leq 1$ sets the width of the filter and δ_g sets the relative wavelength/frequency of the gain peak as

$$\delta_g = (\omega_0 - \omega_g), \tag{18}$$

The IIR filter with frequency response of Eq. (17) corresponds to filter coefficients of,

$$\begin{aligned} a &= \eta \cdot \exp[i(\omega_0 - \omega_g)dt], \\ b &= 1-\eta, \end{aligned} \tag{19}$$

The digital filter is then implemented by updating the field in each subsection as follows:

$$\begin{aligned} E_F(t) &= bE_F(t) + aE_F(t-\Delta t), \\ E_B(t) &= bE_B(t) + aE_B(t-\Delta t). \end{aligned} \tag{20}$$

In addition to accounting for gain dispersion, the wavelength shift in peak gain due to changes in carrier density and temperature cannot be ignored if the model is to accurately predict lasing wavelength. These effects are included as follows:

$$\omega_g(T,N) = \omega_g(N_0,T_0) + \frac{d\omega}{dT}(T-T_0) + \frac{d\omega}{dN}(N-N_0), \tag{21}$$

where $\omega_g(N_0,T_0)$ is the peak of the gain curved as measured at N_0 and T_0, $^{d\omega}/_{dN}$ and $^{d\omega}/_{dT}$ are the rate of change of peak gain with carrier density and temperature respectively, approximated as being linear.

Finally, the tuning dynamics of the laser, namely changes in refractive index due to temperature and carrier density are included. The thermally induced change in effective index is calculated as

$$\Delta n_{eff} = \frac{dn_{eff}}{dT}(T-T_0), \tag{22}$$

where dn_{eff}/dT is the rate of change of effective index with temperature, measured as 2.4×10^{-4}, and T_0 is the reference temperature.

Effective index changes due to the free carrier plasma effect are accounted for via

$$\Delta n_{eff} = \frac{\alpha\lambda}{4\pi}\frac{dg}{dN}(N-N_{tr}), \tag{23}$$

where α is the linewidth enhancement factor [19]. The parameters used in the model are given in Table 1.

3.2. Thermal formulation

The heat conduction equation is given as

$$\frac{\partial T(x,y,z,t)}{\partial t} = \frac{K}{\rho C}\nabla^2 T(x,y,z,t) + \frac{Q(x,y,z,t)}{\rho C}, \tag{24}$$

where T is the temperature, K is the thermal conductivity, C is the specific heat, ρ is the density, and Q is the heat generation. x, y, z correspond to spatial co-ordinates and t is time. In the steady state case we can let

$$\frac{\partial T(x,y,z,t)}{\partial t} = 0, \tag{25}$$

Optics EXPRESS

Table 1. TD-TMM Model Parameters

Parameter	*Symbol and unit*	*Values*
Quantum well thickness	d (μm)	0.03
Waveguide width	w (μm)	2
Non-radiative linear recombination	A (10^8 s^{-1})	1 [c]
Bimolecular recombination	B (10^{-10} cm^3s^{-1})	1 [c]
Auger recombination	C (10^{-30} cm^6s^{-1})	7.0 [c]
Intrinsic loss	α_i (cm^{-1})	28 [b]
Slot loss	α_i	0.1 [a]
Slot reflectivity	r	0.1 [a]
Transparency carrier density	N_{tr} (10^{18} cm^{-3})	1.9 [b]
Differential gain	$^{dg}/_{dN}$ (10^{-15} cm^2)	1.0 [b]
Gain freq. shift with N	$^{d\omega}/_{dN}$ (10^{-6} rad cm^{-3})	2.0 [b]
Gain freq. shift with T	$^{d\omega}/_{dT}$ (10^{12} rad°C^{-1})	2.7 [b]
Linewidth enhancement factor	α	3 [b]
Geometric spontaneous coupling factor	β_g (10^{-4})	1.2 [b]
Fundamental saturation coefficient	ϵ_0 (10^{-16} cm^3)	6 [c]
Group index	n_g	3.6 [c]
Confinement factor	Γ	0.05 [a]
Injection efficiency	η_i	0.8 [b]
Junction Voltage	V_j	0.88 [b]

[a] Calculated
[b] Experimentally measured
[c] Taken from literature

in which case the heat equation reduces to

$$K\nabla^2 T(x, y, z) = -Q(x, y, z, t). \tag{26}$$

The heat generation term in each layer, Q_i is defined for three layer types. For the InP cladding layers we define Q_i is defined as joule heating by

$$Q_i = j^2\rho_i \tag{27}$$

where j is the current density and ρ_i is the ohmic resistivity. For the active region, we follow the approach taken in [20, 21], which give

$$Q_A = \frac{V_j(1 - \eta_{sp} f_{sp})}{d_A}[d_A qR(z) + (j - d_A qR(z))(1 - \eta_i)], \tag{28}$$

where d_A is the height of the AlGaInAs active region, V_j is the junction voltage, η_{sp} and η_i are the internal quantum efficiencies of spontaneous emission and stimulated emission respectively, f_{sp} is the ratio of spontaneous emission absorbed by the cladding layers relative to the total spontaneous emission from the active region. The carrier and photon density profiles solved by the TD-TMM are taken into account via the current density, which is

$$j = qd[g(z)v_g S(z) + R(z)], \tag{29}$$

where $R(z)$ is given previously in Eq. (14) and $g(z)$ and $S(z)$ are the gain and photon density profiles respectively as calculated from the TD-TMM.

Finally, heating from the electrode is also taken into account as

$$Q_g = \frac{j^2\rho_{con}}{d_g}, \tag{30}$$

Optics EXPRESS

where d_g is the thickness of the gold and ρ_{con} is the resistance of the contact. Table 2 shows the values for each of the layers considered in the thermal simulation, where the smallest layers in the epitaxial structure with negligible impact are omitted. The epitaxial structure of the laser can be seen in Fig. 3. The experimental measurements were performed on a probe station with the AlN sub-carrier placed on a copper heat sink. As such, in addition to the physical layers associated with the chip, the air interface between the chip and the copper heat sink must be accounted for. This is done by adding an effective layer between the copper heat sink and AlN carrier, with a thermal resistance calibrated to 4×10^{-4} K m^2 W^{-1}.

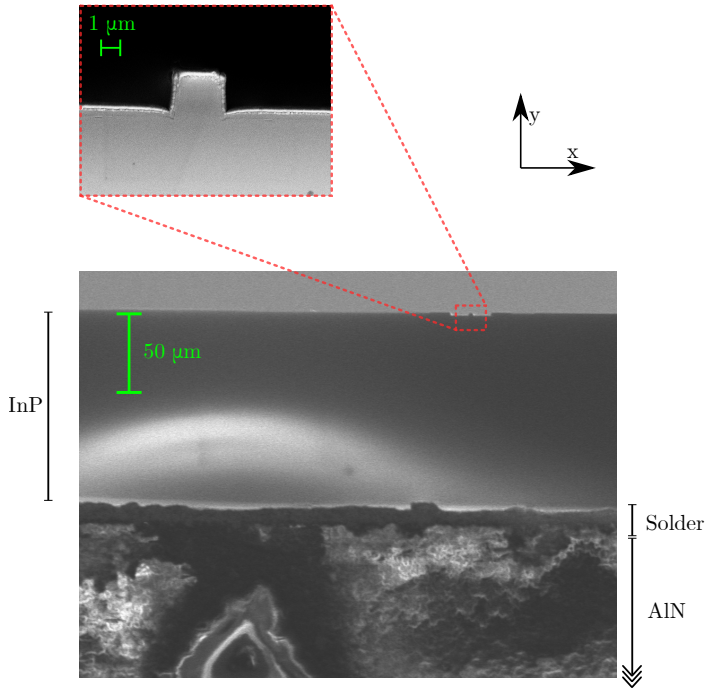

Fig. 3. Scanning electron microscope (SEM) image of a laser face on showing ridge in the upper image, lower image showing thick InP substrate and AlN carrier. Height of different epitaxial layers can be seen, where the solder layer in particular varies along the width of the chip.

Table 2. Physical Parameters for each Layer.

Material	Doping	Height (µm)	Conductivity K (W m^{-1} K^{-1})	Resistivity ρ (Ω m)	Resistance ρ_g (Ωm^2)
Au	–	1	300	–	1.0×10^{-10}
InP	P	1.8	68	7.6×10^{-4}	–
AlGaInAs	–	0.34	5	1×10^{-4}	–
InP	N	120	68	2.4×10^{-4}	–
Solder	–	20	20	–	–
AlN	–	600	180	–	–

Optics EXPRESS

4. Simulation results

4.1. Model verification

In order to verify the accuracy of the numerical model it is first compared to experimental measurements of a simpler two section single-mode slotted laser, the details of which can be found in [7]. First, the model is compared to wavelength measurements of a tuning curve as shown in Fig. 5(a). Second, it is possible to take direct thermal measurements of the surface of the laser via CCD based thermoreflectance imaging (CCD-TR). This method as applied to laser diodes was previously presented in [9]. Figure 4 shows the thermal map obtained from the CCD-TR method of a 400 µm long single mode laser. By performing this measurement over a range of currents the average cavity temperature as a function of injection current is obtained. This experimental result is then compared directly with the simulated temperature as shown in Fig. 5(b).

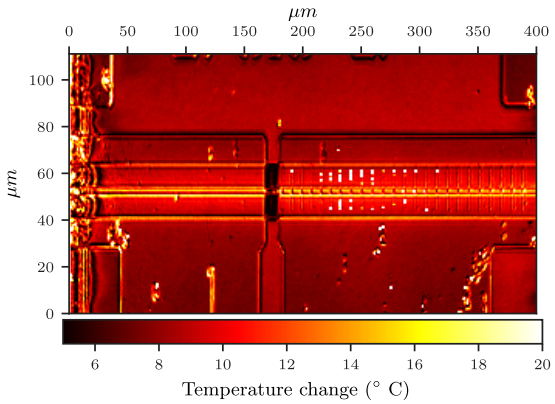

Fig. 4. CCD-TR map of a 400 µm laser at 100 mA corresponding to the measurements in Fig. 5(b). Slots that form the grating can be seen in the front section of the laser. The highest temperatures occur along the ridge. The temperature change was measured relative to a heat-sink temperature of 20 °C.

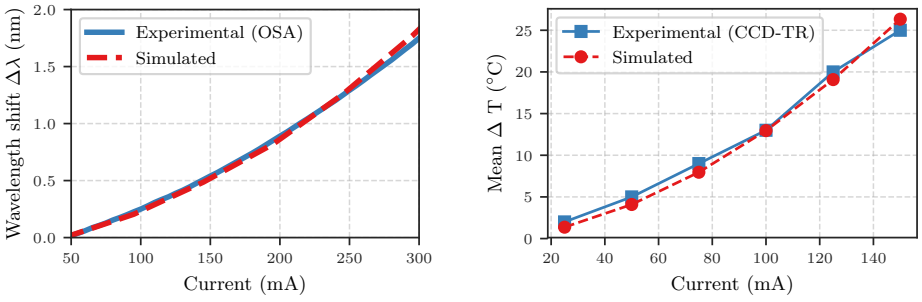

((a)) Optical verification ((b)) CCD-TR verification

Fig. 5. (a) Simulated and measured wavelength shift of a 400 µm cavity length laser. (b) Simulated temperature of a 400 µm slotted laser compared with CCD-TR map in Fig. 4.

Optics EXPRESS

4.2. Vernier tuning

The thermo-optic model is now used to simulate the tuning behaviour of the vernier lasers. A vernier laser with slot periods of 70 µm for the front mirror and 80 µm for the back mirror is simulated. The FSRs are 4.9 nm and 4.3 nm for the front and back mirror, respectively. The gratings both consist of nine slots each. Figure 6(a) shows the experimentally measured wavelength and SMSR maps of the laser, compared with simulated values in Fig. 6(b). Here the gain section is held at 100 mA while the currents to the front and back section are tuned. We emphasize here a clear difference with the SG-DBR laser. The mirror sections in our design have the same active region as the gain section. The tuning wavelength of the simulation is seen to match well with the experimental case reproducing the tuning trends accurately. A "saddle" feature is observed in both cases at front and back current at ~ 100 mA each. Agreement between experiment and simulation demonstrates that the thermo-optic model which we have developed gives an accurate description of the operation of this widely tunable laser. We see a tuning range of nearly 50 nm with supermodes clearly visible in both the experimental and simulation tuning maps.

The tuning regimes can be explained as follows. At lower currents, the front and back section are tuned primarily due to increasing carrier density. As the current to each section increases, the thermal tuning at some point exceeds the carrier density tuning. The midpoint of the "saddle" feature corresponds to the currents at which both carrier and thermal tuning are approximately equal to one another, beyond which thermal tuning begins to dominate. This tuning pattern results in a limiting factor for efficiency, in so far as the tuning between channels must be in regions with injection current ≥ 100 mA. Once above 100 mA however, the tuning process is still rather inefficient requiring ≥ 250 mA in order to tune to certain channels. Examining the simulated profile of the cavity in detail can shed light on this tuning behaviour.

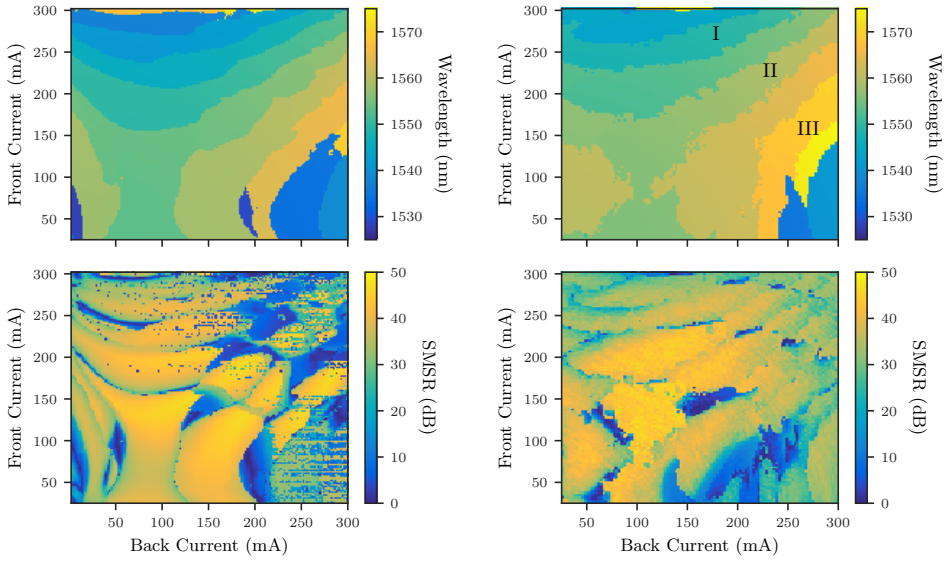

((a)) Experiment ((b)) Simulation

Fig. 6. (a) Experimental and (b) simulated tuning map of wavelength (top) and SMSR (bottom). The random speckles in the SMSR map in (a) are a result of stability issues with measurement setup due to fibre coupling.

Optics EXPRESS

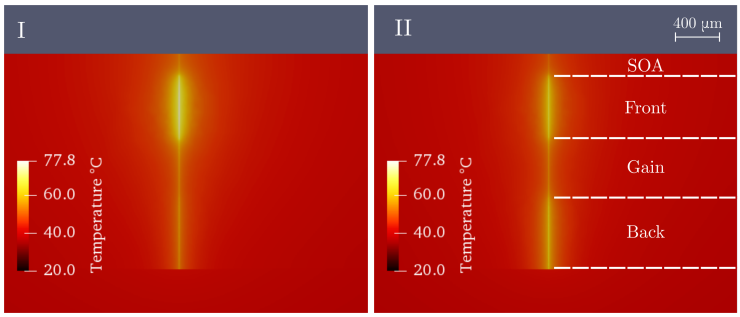

((a)) Front 265 mA, back 180 mA ((b)) Front 220 mA, back 230 mA

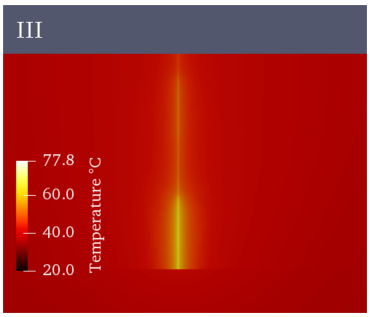

((c)) Front 150 mA, back 264 mA

Fig. 7. Simulated temperature distributions for the three supermodes labelled in Fig. 6(b).

Consider the current co-ordinates shown by Roman numerals on Fig. 6(b), which correspond to three distinct supermodes. For each of these co-ordinates we have simulated the thermal, carrier and photon density profiles along the cavity. Figure 7 shows the surface of the laser as calculated via the FEM. The thermal tuning required to tune between super-modes leads to very high temperatures in the gratings, reaching up to ~ 77 °C.

Extracting the profiles along the cavity gives the photon density carrier density and temperature as plotted in Fig. 8. This plot reveals a prohibitive consequence of direct current injection on tuning efficiency. The carrier density in Fig. 8(b) is seen to increase with mirror injection current. This is in contrast to the usual approximation that the carrier density is constant once the laser is above threshold. This is due to the fact that the radiation loss within the mirror sections is quite large; a result of etching deep slots. As such, the gain is not saturated within the gratings and the carrier density can increase with injection current. The increase in carrier density results in a negative change in the effective refractive index due to the free carrier plasma effect which counteracts the positive refractive index change induced via thermal tuning. The two tuning effects are counterbalancing one another reducing the overall efficiency of the thermal tuning, resulting in the high injection currents and temperatures required.

Considering the tuning of the front grating in Fig. 8 from I to III, we can calculate the contribution to the refractive index change from the individual physical effects, as can be seen in Fig. 9(a). Despite the high injection current the carrier density induced Δn_{eff} is still significant, reducing the efficiency of the thermal tuning to a large degree. Figure 9 shows the effect of loss on carrier induced tuning. In the ideal case with $\alpha_s = 0$ the tuning contribution is less than in the $\alpha_s = 0.1$ case. From this it can be concluded that reducing loss in the gratings is a path to

Optics EXPRESS

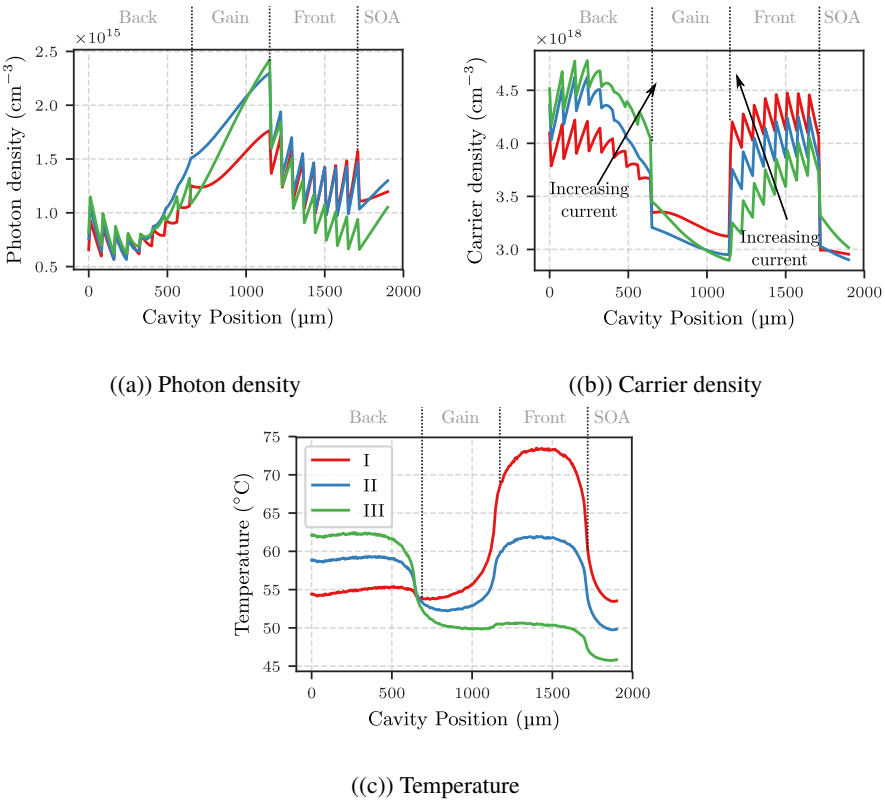

((a)) Photon density

((b)) Carrier density

((c)) Temperature

Fig. 8. Simulated profiles in the laser cavity for the three supermodes labelled in Fig. 6(b), (a) photon density, (b) carrier density, (c) temperature. The Front/Back section currents for I, II and III are 265/180, 220/230 and 150/264 mA respectively with a constant gain and SOA current of 120 mA and 30 mA respectively. The sharp peaks observed in the front and back grating photon and carrier densities correspond to the slot positions.

improving tuning efficiency.

A further consequence of this high carrier density is a reduced SMSR observed in both simulation and experiment at higher grating current. As spontaneous emission $R_{sp} \propto N^2$ we can expect such a reduction at high grating currents as more spontaneous emission is coupled into the cavity. Thus, it is necessary to alter the slotted laser design to produce more efficient tuning.

4.3. Linewidth

The linewidth of widely tunable lasers is another parameter which is of importance in particular for coherent communications. When using high order modulation formats, such as 16-QAM, low laser linewidth is crucial in achieving error free transmission [22]. Given that the Vernier lasers have relatively long cavity lengths in excess of 1500 µm one anticipates a relatively low linewidth, which is inversely proportional to the cavity length. Contrary to this expectation the linewidth experimentally measured from such Vernier lasers was at best ~ 2 MHz. The cause of this was not fully understood and whether this was due to device fabrication or inherent to the design. In order to gain an insight into this we apply the TD-TMM thermo-optic model as a diagnostic tool to simulate the theoretical linewidth performance compared with the experimentally measured

Optics EXPRESS

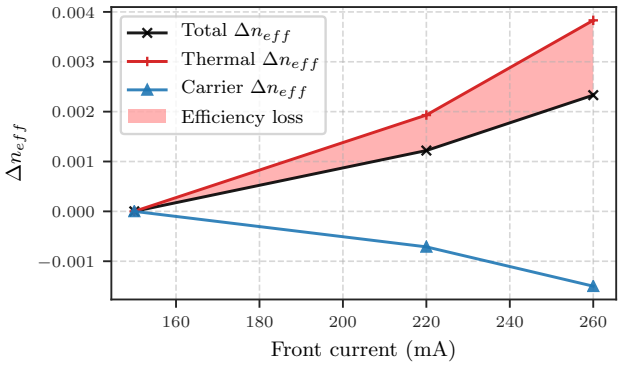

((a)) .

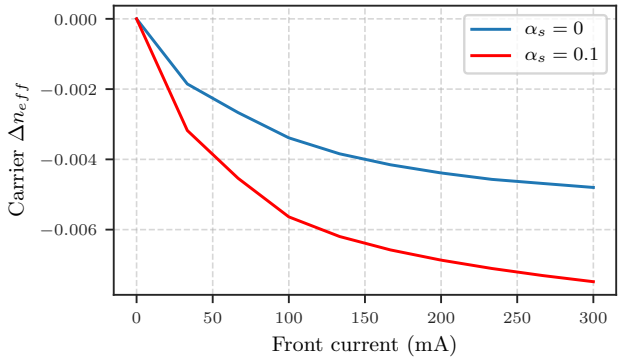

((b))

Fig. 9. (a) Individual contribution of thermal and carrier effects to the overall tuning for the front grating. Currents in (a) follow those points highlighted by roman numerals in Fig. 6(b). (b) Comparison between slots with loss and ideal slots with no loss. The loss in the slots is seen to increase the carrier density tuning. Back grating current is constant in at 200 mA in (b).

linewidth. The grating period of this laser is 52 µm for the front mirror and 57 µm for the back mirror, which leads to FSRs of 6.6 nm and 6.02 nm, respectively. This laser was measured to have eleven wavelength channels which it could be tuned to, each channel having good SMSR > 30 dB from 1520 nm to 1570 nm [8]. Taking the 1525 nm channel which was tuned with front and back currents of 75 mA each, a gain section current of 120 mA and an SOA current of 30 mA; the linewidth was measured using the self-heterodyne method. The thermo-optic model was then run with the same injection currents, the resulting spectrum correctly predicting the laser channel as shown in Fig. 10. The TD-TMM was then run for sufficient iterations in order to attain a good frequency resolution of the line-shape from which the FWHM was extracted via a Lorentzian fit. The results of this are shown in Fig. 11(a). The simulation predicts a higher linewidth of 5.96 MHz compared with the experimentally measured value of 4.97 MHz. Importantly, the relatively wide linewidth was reproduced in the simulation. We also consider a second wavelength channel tuned to approximately the centre of the C-band at 1545 nm. The comparison between simulation and experiment is seen in Fig. 11(b). The simulation in this case

Optics EXPRESS

provides a closer match with experiment predicting a FWHM of 7.36 MHz versus the measured 7.16 MHz.The broad linewidth found in experiment and simulation implies that the vernier slotted laser design requires alterations in order to achieve linewidth on the order of 1 MHz or less. Specifically this paper has highlighted the high carrier density and as a result increased spontaneous emission as a root cause which can be addresses in future designs. The loss within the grating is another contributory factor leading to high tuning currents and as such this loss requires further grating and slot optimization to be reduced.

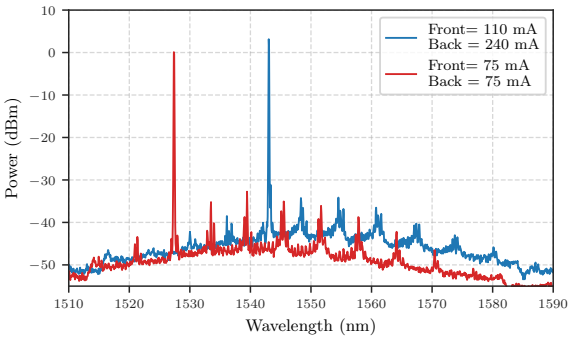

Fig. 10. Simulated lasing spectrum of a vernier slotted laser tuned to two different channels.

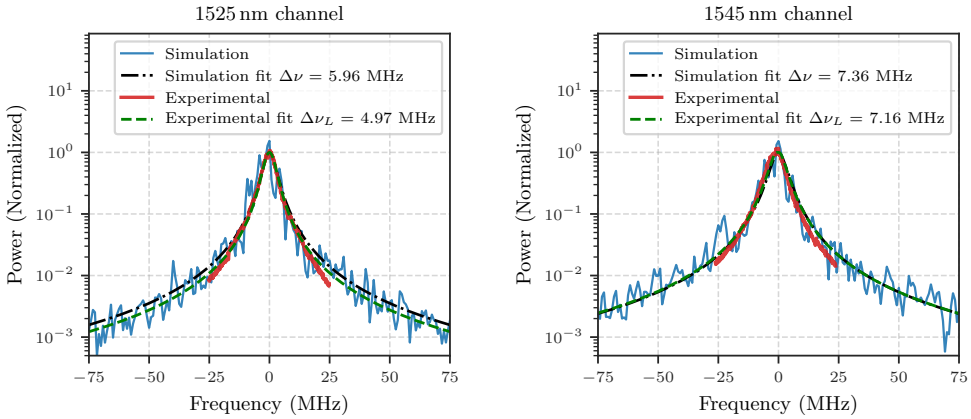

((a)) ((b))

Fig. 11. Experimental and simulated linewidth of a vernier slotted laser with (a) both front and back currents of 75 mA and (b) front and back currents of 110 mA and 240 mA respectively; gain section current of 120 mA in each case.

5. Conclusion

We have developed a widely tunable laser covering the C-band with simple fabrication and no re-growth. In operation, it requires significant currents in the front and back mirror sections to cover the full tuning range. We developed a thermo-optic model to fully describe the tuning

Optics EXPRESS

behaviour and very good agreement is shown with the experimental tuning and SMSR maps. A key feature of these lasers is the very high carrier densities in the mirror sections. This leads to inefficient tuning where carrier and thermal effects are competing and reducing the laser performance. This leads also to relatively broad linewidths. In future designs, we will look at ways in which the tuning performance and lower linewidths can be improved. The industry standard SG-DBR laser requires a current of less than 20 mA for front and back mirror sections to cover the same tuning range. So, a significant improvement is now required in our designs to achieve improved performance. Recently, a key development is the fabrication of high-order surface grating lasers with standard UV lithography [23]. This should lead the way to greater penetration of the slotted laser designs featuring simple fabrication in commercial DBR fabrication.

Funding

Science Foundation of Ireland (15/IA/2854, 13/RC/2077); CONNECT (13/RC/2077); European Union's Horizon 2020 research and innovation program (713567).

References

1. V. Jayaraman, Z. M. Chuang, and L. A. Coldren, "Theory, design, and performance of extended tuning range semiconductor lasers with sampled gratings," IEEE J. Quantum Electron. **29**, 1824–1834 (1993).
2. A. J. Ward, G. Busico, N. D. Whitbread, L. Ponnampalam, J. P. Duck, and D. J. Robbins, "Linewidth in widely tunable digital supermode distributed bragg reflector lasers: Comparison between theory and measurement," IEEE J. Quantum Electron. **42**, 1122–1127 (2006).
3. H. Abe, S. G. Ayling, J. H. Marsh, R. M. De La Rue, and J. S. Roberts, "Single-mode operation of a surface grating distributed feedback gaas-algaas laser with variable-width waveguide," IEEE Photonics Technol. Lett. **7**, 452–454 (1995).
4. H. Yang, P. Morrissey, W. Cotter, C. L. M. Daunt, J. O'Callaghan, B. Roycroft, N. Ye, N. Kelly, B. Corbett, and F. H. Peters, "Monolithic integration of single facet slotted laser, soa, and mmi coupler," IEEE Photonics Technol. Lett. **25**, 257–260 (2013).
5. Q. Lu, A. Abdullaev, M. Nawrocka, W. Guo, J. O'Callaghan, and J. F. Donegan, "Slotted single mode lasers integrated with a semiconductor optical amplifier," IEEE Photonics Technol. Lett. **25**, 564–567 (2013).
6. Q. Lu, W. Guo, M. Nawrocka, A. Abdullaev, C. Daunt, J. O'Callaghan, M. Lynch, V. Weldon, F. Peters, and J. F. Donegan, "Single mode lasers based on slots suitable for photonic integration," Opt. Express **19**, B140–B145 (2011).
7. A. Abdullaev, Q. Lu, W. Guo, M. J. Wallace, M. Nawrocka, F. Bello, A. Benson, J. O'Callaghan, and J. F. Donegan, "Improved performance of tunable single-mode laser array based on high-order slotted surface grating," Opt. Express **23**, 12072–12078 (2015).
8. M. Nawrocka, Q. Lu, W.-H. Guo, A. Abdullaev, F. Bello, J. O'Callaghan, T. Cathcart, and J. F. Donegan, "Widely tunable six-section semiconductor laser based on etched slots," Opt. Express **22**, 18949–18957 (2014).
9. M. Wallace, R. O. Meehan, R. Enright, F. Bello, D. McCloskey, B. Barabadi, E. Wang, and J. F. Donegan, "Athermal operation of multi-section slotted tunable lasers," Opt. Express **25**, 14414–14426 (2017).
10. F. Bello, M. J. Wallace, R. McKenna, G. Jain, Q. Y. Lu, W. H. Guo, and J. F. Donegan, "Athermal tuning for a two-section, all-active dbr laser with high-order grating," IEEE Photonics J. **10**, 1–11 (2018).
11. Q. Lu, W. Guo, A. Abdullaev, M. Nawrocka, J. O'Callaghan, M. Lynch, V. Weldon, and J. Donegan, "Re-growth free single mode lasers based on slots suitable for photonic integration," in *2012 14th International Conference on Transparent Optical Networks (ICTON),* (IEEE, 2012), pp. 1–4.
12. Q. Lu, W. Guo, R. Phelan, D. Byrne, J. Donegan, P. Lambkin, and B. Corbett, "Analysis of slot characteristics in slotted single-mode semiconductor lasers using the 2-d scattering matrix method," Photonics Technol. Lett. IEEE **18**, 2605–2607 (2006).
13. M. S. Alnæs, J. Blechta, J. Hake, A. Johansson, B. Kehlet, A. Logg, C. Richardson, J. Ring, M. E. Rognes, and G. N. Wells, "The fenics project version 1.5," Arch. Numer. Softw. **3**, 9–23 (2015).
14. A. Logg, K.-A. Mardal, and G. N. Wells, *Automated Solution of Differential Equations by the Finite Element Method* (Springer, 2012).
15. L. Coldren, S. Corzine, and M. Mashanovitch, *Diode Lasers and Photonic Integrated Circuits* (Wiley, 2011).
16. M. Davis and R. O'Dowd, "A new large-signal dynamic model for multielectrode dfb lasers based on the transfer matrix method," Photonics Technol. Lett. IEEE **4**, 838–840 (1992).
17. X. Han, J. Gao, H. Wang, and Y. Yu, "Thermal analysis of an soa integrated in sg-dbr laser module," in *2015 International Conference on Numerical Simulation of Optoelectronic Devices (NUSOD),* (IEEE, 2015), pp. 107–108.
18. H. Saidi, M. Msahli, R. B. Dhafer, and S. Ridene, "Self-consistent optimization of [111]-algainas/inp mqws structures lasing at 1.55Âăum by a genetic algorithm," Superlattices Microstruct. **112**, 200–209 (2017).

Optics EXPRESS

19. W. Li, W.-P. Huang, and X. Li, "Digital filter approach for simulation of a complex integrated laser diode based on the traveling-wave model," IEEE J. Quantum Electron. **40**, 473–480 (2004).
20. X. Han, J. Gao, H. Wang, and Y. Yu, "Thermal analysis of an soa integrated in sg-dbr laser module," in *2015 International Conference on Numerical Simulation of Optoelectronic Devices (NUSOD),* (IEEE, 2015), pp. 107–108.
21. T. Kobayashi and Y. Furukawa, "Temperature distributions in the gaas-algaas double-heterostructure laser below and above the threshold current," Jpn. J. Appl. Phys. **14**, 1981 (1975).
22. S. J. Varughese, V. Mathew, S. Swain, D. Venkitesh, and R. David Koilpillai, "200g system with pdm-16qam: Performance evaluation and trade-offs," in *2015 Twenty First National Conference on Communications (NCC),* (IEEE, 2015), pp. 1–6.
23. M. Wang, H. Wang, P. Ma, F. Dong, A. Liu, and W. Zheng, "Eight-channel laser array with 100 GHz channel spacing based on surface-slotted structures fabricated by standard lithography," Opt. Lett. **43**, 4867–4870 (2018).